

Aggregation of magnetic nanoparticles functionalized with trans-resveratrol in aqueous solution

Thi-Nga Nguyen

UMR IATE, University of Montpellier, Institut Agro, INRAE

Quang-Hung Tran

eV-Technologies

Clarence Charnay

Institut Charles Gerhardt UMR 5253 CNRS-UM, Université de Montpellier

Xavier Dumail

Institut Charles Gerhardt UMR 5253 CNRS-UM, Université de Montpellier

Corinne Reibel

Institut Charles Gerhardt UMR 5253 CNRS-UM, Université de Montpellier

Guillaume Cazals

IBMM UMR5247, CNRS, ENSCM, Université de Montpellier

Gilles Valette

IBMM UMR5247, CNRS, ENSCM, Université de Montpellier

Christian Jay-Allemand

UMR IATE, University of Montpellier, Institut Agro, INRAE

Ferial Terki

PhyMedExp UMR CNRS 9214 – Inserm U1046

Luc P. R. Bidel (✉ luc.bidel@inrae.fr)

UMR AGAP, University of Montpellier, CIRAD, INRAE, Institut Agro

Research Article

Keywords: nanoparticle aggregation, trans-resveratrol, magnetic nanoparticles, mesoporous silica shells, functionalization nanoparticles.

Posted Date: January 31st, 2022

DOI: <https://doi.org/10.21203/rs.3.rs-1300084/v1>

License:   This work is licensed under a Creative Commons Attribution 4.0 International License.

[Read Full License](#)

Additional Declarations: No competing interests reported.

Version of Record: A version of this preprint was published at Discover Nano on April 19th, 2023. See the published version at <https://doi.org/10.1186/s11671-023-03805-9>.

Abstract

In the framework of a protein-ligand-fishing strategy to identify proteins that bind to *trans*-resveratrol, a natural phenolic compound with pharmacological benefits, we have developed magnetic nanoparticles covalently linked to *trans*-resveratrol through three different derivatives and examined their aggregation behavior in aqueous solution. The monodispersed magnetic core (18 nm) with its mesoporous silica shell (93 nm) exhibited a notable superparamagnetic behavior useful for magnetic bioseparation. The hydrodynamic diameter, deduced from dynamic light scattering analysis, of the nanoparticle increased from 100 to 800 nm when the aqueous buffer changed from pH 10.0 to 3.0. A size polydispersion occurred from pH 7.0 to 3.0. In parallel, the value of the extinction cross-section increased according to a negative power law of the UV wavelength. This was mainly due to light scattering by mesoporous silica, whereas the absorbance cross-section remained very low in the 230-400 nm domain. The three types of resveratrol-grafted magnetic nanoparticles exhibited similar scattering properties, but their absorbance spectrum was consistent with the presence of *trans*-resveratrol. Their functionalization increased their negative zeta potential when pH increased from 3.0 to 10.0. The mesoporous nanoparticles were monodispersed in alkaline conditions, where their anionic surface strongly repulsed each other but aggregated progressively under van der Waals forces and hydrogen bonding when negative zeta potential decreased. The characterized results of nanoparticle behavior in aqueous solution provide critical insight for further study of nanoparticles with proteins in biological environment.

1. Introduction

Phenolic compounds interact with many peptides and proteins and modulate metabolism (1), signaling pathways (2, 3), and reactions of organisms to environmental cues and bio-aggressors (4). Among phenolic compounds, *trans*-resveratrol (3,5,4'-trihydroxystilbene) is the main monomer of the stilbenoid subclass. Produced by plant species, it is considered with an increasing interest in many biological fields related to biocontrol (5), cosmetic (6, 7), nutrition and medicine (8-10). Among the 11987 interactions between 369 polyphenols and 5699 unique proteins annotated in the STITCH interactome database, *trans*-resveratrol is referenced in 738 interactions at the 4th rank of the highest interacting phenolic compound (1). Identification of new peptide and protein targets of *trans*-resveratrol is an essential step to elucidate their mechanism of action as fungistatic and fungicide (11, 12), bacteriostatic and bactericide (13), antioxidant, and many healthy properties reviewed (14): vasorelaxant agent, anti-hypertensive and cardioprotective agent, estrogeno-mimetic agent, anti-diabetic agent, peptide anti-aggregative agent, and neuroprotective agent, anti-inflammatory agent, anti-angiogenic agent, immunomodulatory agent, antitumor drug, radioprotective agent. To improve the bioavailability of this poorly soluble *trans*-resveratrol, many efforts have been carried out for vectorizing it into various vehicles reviewed such as vesicular systems (nano-emulsion, nano-micelles, cyclodextrin complexes) (15-17), and nanocarriers (solid lipid nanoparticles, nano-suspensions, nano-capsules, protein-based or chitosan-based nanoparticles) (18). Recently, mesoporous silica nanoparticles have been used as a nanocarrier of adsorbed *trans*-resveratrol for active targeted delivery with progressive release (19-21). Furthermore,

magnetic iron oxide nanoparticles functionalized by an organosilane coupling agent (3-chloropropyltriethoxysilane, CPTES) have been used as *trans*-resveratrol a nanovector (22).

Nanoparticle designing for protein-ligand-fishing remains challenging. Among the diversity of magnetic nanoparticle available (iron, nickel, cobalt), some iron oxide nanoparticles exhibit superparamagnetic property in the temperature range of living cells when they are submitted to an external magnetic field, without remanence left when the field is removed. Compared to ferromagnetic permanent nano-magnet, they exhibit higher magnetic susceptibility and lower aggregation tendency. They are more suitable to monitor protein-ligand-fishing (23). Parameters such as their size, shape, coating, functionalization, and zeta-potential can have a great impact on their diffusion, uptake capacity, toxicity and affinity for their target, their colloidal stability in aqueous proteins necessary for preserving native proteins. The aggregation behavior in aqueous condition appears as a critical phase to determine how to use it. Although there are researches on the aggregation of iron oxide nanoparticle^{12,13} but the functionalized magnetic nanoparticle is rarely documented. Indeed, the properties of functionalized nanoparticles should be carefully characterized to avoid any undesirable activity and further understanding for later uses¹⁵.

Here, we report the impact of pH to the aggregation of magnetic nanoparticle grafted with *trans*-resveratrol. Initially, we present the synthesis and physical characterizations of superparamagnetic iron oxide core with a high magnetic moment, the synthesis of its mesoporous silica shell, the synthesis of three silanized resveratrol derivatives, and their grafting on silica shell. To examine *trans*-resveratrol covalent grafting on magnetic nanoparticles (MNPs), FT-IR, and UV-Vis were used. We further analyze the impact of pH on the aggregation of the three resveratrol derivatives grafted MNPs (**CS1**, **CS2**, and **CS3**). This MNPs-resveratrol system is the first result to develop new studies toward quantification of grafting ligand on nanoparticles and screening of specific proteins for *trans*-resveratrol by ligand fishing.

2. Materials And Methods

Synthesis of magnetic core

Nanoparticles were synthesized by the decomposition method (24). The flask contains 5.055 g *n*-docosane (99 %, Acros Organic), 0.181 g iron oxide hydrate (catalyst grade, 30-50 Mesh, Sigma Aldrich), and 3 g oleic acid (>99 %, Sigma Aldrich). The mixture was put under vacuum for 30 minutes, then heated under reflux to 340°C under argon gas for 1h30m. The mixture was then dissolved in *n*-pentane (for analysis RPE) and diethyl ether/ethanol (2:1). Nanoparticles were collected by centrifugation and washed with diethyl ether/ethanol 2:1. Finally, all nanoparticles were dissolved in 15 mL CHCl₃ (RPE for analysis) and 200 µL oleylamine, then stored at 4°C.

Enwrapping of a magnetic core with a mesoporous silica shell

The formation of the silica shell was carried out with tetraethylorthosilicate (TEOS) agent (25). The flask containing 0.125 g cetyltrimethylammonium bromide (CTAB) ($\geq 98\%$, Sigma Aldrich), 60 mL pure water (for HPLC, Sigma Aldrich), and 440 μL NaOH 2M was stirred at 70°C for 1h. The iron oxide core in CHCl_3 (11 x 100 μL) was then added at 3-4 min intervals. The mixture was stirred at 80°C for 1h30 before the addition of 100 μL of TEOS ($\geq 99\%$ (GC), Sigma Aldrich), followed by another addition of 500 μL TEOS 30 min later. The mixture was kept at 80°C for another 1h30 period. Nanoparticles were collected by centrifugation at 20 rpm for 15 minutes (Allegra64R centrifuge, Beckman coulter, USA), then suspended in 0.075M NH_4NO_3 for one night. Nanoparticles were washed with absolute ethanol (99%, VWR) and pure water before being dried under vacuum.

Each batch of nanoparticles was examined using Transmission Electronic Microscopy (TEM) and morphometric measurements were carried out with magnification at 15000x and 50000x using a JEOL 1200 EXII microscope (Japan). Magnetic data were collected with a Quantum Design MPMS-XL SQUID magnetometer working in the temperature range 5-300 K.

Silanization of trans-resveratrol

To graft *trans*-resveratrol on the surface of core/shell nanoparticle, silane-*trans*-resveratrol derivatives were synthesized by the base-catalyzed reaction of (triethoxysilyl)propyl isocyanate with *trans*-resveratrol in tetrahydrofuran THF shown in Scheme 3.1.

1.14 g *trans*-resveratrol (5 mmol, $> 99\%$, TCI Europe) and 2.50 mL 3-(triethoxysilyl)propyl isocyanate (10 mmol, 95%, Sigma) were dissolved in 20 mL dry THF, then 70 μL N,N-diisopropylethylamine ($> 99\%$, TCI Europe) was added. The reaction was stirred under reflux at 70°C for 3 days. The reaction was followed by infrared spectroscopy and thin layer chromatography (TLC) using pre-coated TLC sheets with UV fluorescent silica gel (Merck 60F254). The solvent was then removed under reduced pressure and the mixture of **(1)**, **(2)**, and **(3)** was purified by flash chromatography (Isolera One, Biotage, Sweden) using a Biotage SNAP ULTRA column and *n*-hexane/acetone 2:1 as eluent, to give **1** (50%), **2** (30%), **3** (16%).

To elucidate the structures of **1**, **2**, and **3**, NMR spectra were measured in $\text{DMSO}-d_6$, using a Bruker Avance 400 MHz spectrometer. Chemical shifts (δ) were expressed in ppm relative to tetramethyl silane (TMS) and coupling constants (J) in Hz. Mass spectra were obtained using a Synapt G2-S high-definition mass spectrometry system (Waters Corp., Milford, MA) equipped with an electrospray ionization (ESI) source. Since compound **1** did not ionize well in the ESI source, its mass spectrum was obtained using a Bruker RapifleX MALDI TOF spectrometer (Bruker Daltonik GmbH, Bremen, Germany) equipped with a Smartbeam 3D laser. The MALDI TOF analysis was performed in positive ion reflectron mode over a mass range of m/z 450 -3000 with or without cationization agent. The matrix (DHB, 10 $\text{g}\cdot\text{L}^{-1}$) and the sample were mixed (10:1 v/v) and 1 μL of the mixture was spotted onto the MALDI target plate and air dried. For the experiments with a cationizing agent, 1 μL of 10 $\text{g}\cdot\text{L}^{-1}$ sodium trifluoroacetate was added to the mixture before spotting.

¹H-NMR of 1: δ ppm (400 MHz, DMSO-*d*₆, Me₄Si): 7.81 (m, 3H, N-H), 7.60 (d broad, *J* = 8 Hz, 2H, H-3', H-5'), 7.32 (d, *J* = 16 Hz, 1H, H-α), 7.20 (m, 3H, H-β, H-2', H-6'), 7.11 (d, *J* = 8 Hz, 2H, H-2, H-6), 6.76 (t, *J* = 2 Hz, 1H, H-4), 3.77 (q, *J* = 6 Hz, 18H, -Si-O-CH₂-CH₃), 3.05 (q, *J*₁ = 4 Hz, *J*₂ = 8 Hz, 6 H, -Si-CH₂-CH₂-CH₂-N), 1.54 (dt, *J*₁ = 4 Hz, *J*₂ = 8 Hz, 6H, -Si-CH₂-CH₂-CH₂-N), 1.17 (m, 27H, -Si-O-CH₂-CH₃), 0.59 (t, *J* = 6 Hz, 6H, Si-CH₂-CH₂-CH₂-N). **¹³C-NMR:** δ ppm (101 MHz, DMSO-*d*₆, Me₄Si) 154.0 (C=O), 151.7 (C-3, C-5), 150.8 (C-4'), 138.9 (C-1'), 133.5 (C-3', C-5'), 129.1 (Cβ), 127.4 (C-α), 126.7 (C-1), , 122.0 (C-2', C-6'), , 116.2 (C-2, C-6), 114.6 (C-4), 57.7 (Si-O-CH₂-CH₃), 54.9 (NH-CH₂-CH₂-CH₂-Si), 22.8 (NH-CH₂-CH₂-CH₂-Si), 18.2 (Si-O-CH₂-CH₃), 7.2 (NH-CH₂-CH₂-CH₂-Si). HRMS (ESI) for C₄₄H₇₅N₃O₁₅Si₃ [(M + formic acid) - H]⁺: m/z calc. 1014.4514. MALDI-TOF [M + Na] m/z 992.4.

¹H-NMR of 2: δ ppm (400 MHz, DMSO-*d*₆, Me₄Si): 9.65 (s, 1H, 3-OH), 7.76 (s broad, 2H, -NH), 7.64-7.56 (m, 2H, H-3', H-5'), 7.18-7.08 (m, H-2', H-6', H-α, H-β), 6.80 (m, 2H, H-2, H-6), 6.41 (t, *J* = 2 Hz, 1H, H-4), 3.76 (t, *J* = 7 Hz, 12H, -Si-O-CH₂-CH₃), 3.05 (t, *J*₁ = 7.5 Hz, *J*₂ = 4 Hz, 4H, -Si-CH₂-CH₂-CH₂-N), 1.53 (m, 4H, -Si-CH₂-CH₂-CH₂-N), 1.16 (m, 18H, -Si-O-CH₂-CH₃), 0.59 (m, 4H, Si-CH₂-CH₂-CH₂-N). **¹³C-NMR:** δ ppm (101 MHz, DMSO-*d*₆, Me₄Si) 158.2 (C-5), 154.3 (C-3), 154.2 (C=O), 150.7 (C-4'), 138.9 (C-1'), 133.6 (C-1), 128.1 (C-β), 127.7 (C-5'), 127.3 (C-3'), 122.0 (C-α), 115.8 (C-2'), 115.6 (C-6'), 110.4 (C-2), 110.2 (C-6), 108.4 (C-4), 57.7 (Si-O-CH₂-CH₃), 43.2 (NH-CH₂-CH₂-CH₂-Si), 23.5 (NH-CH₂-CH₂-CH₂-Si), 18.1 (Si-O-CH₂-CH₃), 7.2 (NH-CH₂-CH₂-CH₂-Si). HRMS (ESI) for C₃₄H₅₄N₂O₁₁Si₂ [M - H]⁺: m/z calc. 721.3196. MALDI-TOF [M + Na + H]⁺ m/z 745.3.

¹H-NMR of 3: δ ppm (400 MHz, DMSO-*d*₆, Me₄Si): 9.24 (s, 2H, 3-OH, 5-OH), 7.76 (t, *J* = 6 Hz, 1H, -NH-CO), 7.57 (t, *J* = 8 Hz, 2H, H-3', H-5'), 7.09-7.02 (m, 4H, H-α, H-β, H-2', H-6'), 6.44 (m, 2H, H-2, H-6), 6.17 (t, *J* = 2 Hz, 1H, H-4), 3.77 (t, *J* = 7 Hz, 6H, -Si-O-CH₂-CH₃), 3.05 (t, *J* = 7 Hz, 2H, N-CH₂-CH₂-CH₂-Si), 1.53 (q, *J* = 6 Hz, 2H, -N-CH₂-CH₂-CH₂-Si), 1.18 (t, *J* = 7 Hz, 9H, -Si-O-CH₂-CH₃), 0.59 (t, *J* = 6 Hz, 4H, N-CH₂-CH₂-CH₂-Si). **¹³C-NMR:** δ ppm (101 MHz, DMSO-*d*₆, Me₄Si) 159.2 (C-3, C-5), 154.9 (C=O), 151.0 (C-4'), 139.4 (C-1'), 134.5 (C-1), 129.3 (C-β), 127.8 (C-3', C-5'), 127.6 (C-α), 122.5 (C-2', C-6'), 105.3 (C-2, C-6), 102.9 (C-4), 58.4 (Si-O-CH₂-CH₃), 43.8 (NH-CH₂-CH₂-CH₂-Si), 23.5 (NH-CH₂-CH₂-CH₂-Si), 18.8 (Si-O-CH₂-CH₃), 7.8 (NH-CH₂-CH₂-CH₂-Si). HRMS (ESI) for C₂₄H₃₃NO₇Si [M - H]⁺: m/z calc. 474.1947. MALDI-TOF [M + Na + H]⁺ m/z 498.2

Functionalized nanoparticles preparation

Three flasks, each containing 100 mg of core/shell (**CS**) nanoparticles, were added with 1 mL toluene (ACS reagent, Sigma Aldrich). Three other flasks contained 150 mg of **1**, **2**, and **3**, respectively, in 1 mL toluene. The 1 mL suspensions of **CS** nanoparticles were added to the latter flasks along with 60 μL of ultrapure water (18.5 MΩ) then stirred and heated up to 70°C for 15 hours. The functionalized **CS1**, **CS2** and **CS3** nanoparticles were then collected by washing with ethanol and drying under vacuum for 3 – 4 hours.

The successful grafting of **1**, **2** and **3** on **CS** was verified by recording the UV and IR absorption spectra of **CS1**, **CS2**, and **CS3** using a UV-1800 spectrometer (Shimadzu, Japan) with 10 mm quartz cuvettes (101-QS, Hellma™, Germany), and a Spectrum Two FT-IR spectrometer (Perkin Elmer, England) in transmittance mode with KBr discs.

Hydrodynamic diameter

The distribution of hydrodynamic diameter (d_H) of the nanoparticles was studied at 25°C by Dynamic Light Scattering (DLS) using a Zetasizer Nano-ZS (Malvern Instruments Limited, UK), adapted to assess particle sizes between 5 and 1000 nm. The instrument was equipped with a 633 nm diode laser and a DTS1070 cell. DLS was analyzed at the back scattering angle of 173°. In this configuration, the contributions of rotational diffusion effects in the observed autocorrelation profiles can be neglected and the translational diffusion coefficient, D , can be assessed (26). Five replicates of each colloidal suspension were homogenized by an ultrasound bath for 5 min and were immediately analyzed by Zetasizer Nano-ZS over 3 min.

Zeta-potential

Zeta potential was also measured with the Zetasizer Nano-ZS. An electric field of 120V was applied across the DTS1060C zeta cell and the electrophoretic mobility of the colloidal suspension was then measured by Laser Doppler Velocimetry (LDV). The zeta potential is referred to as the electrostatic charge at the splining plane boundary separating ions within the diffuse layer which moves with the nanoparticles, and ions that remain with the bulk water, corresponding to the Stern shell. Zeta potential is related to the surface electrostatic charge of nanoparticles ²⁴¹.

Spectrophotometric analyses

For extinction cross-section determination, all nanoparticles were initially suspended in absolute ethanol and were then diluted at the final suspension concentration of 50 ppm (50 µg/mL) in aqueous tris (hydroxymethyl)aminomethane (Tris) buffer (50 mM), previously adjusted to pH 3.0, 5.0, 7.0, and pH 10.0 with HCl 37% and HCl 0.1 N. Extinction was recorded by Enspire microplate reader (PerkinElmer, Singapore) at 1 nm step in front face configuration using 96 wells black microplates (UV-Star µClear, Greiner-Bio-One, Germany) set up at 27 °C.

3. Results

3.1. Characterization of magnetic core and core/shell nanoparticles

As shown in **Figure 1A**, the magnetic core and core/shell particles were fabricated by the decomposition of iron oxide hydrate and sol-gel reaction with tetraethyl orthosilicate, respectively (24).

These nanoparticles were inspected using TEM imaging (**Figure 1B** and **1C**). TEM images showed that core/shell particles are significantly larger than core particles, both being monodispersed. A single core magnetic core was observed, at the center of a porous silica shell. **Figure 1D** shows the size distribution of the MNPs and core/shell particles, determined from TEM images at low magnification images. It evidences a narrow size distribution for both particle types, the mean size of MNPs and core/shell being determined about 18 nm and 93 nm, respectively.

To understand the magnetic properties of these particles, the hysteresis loop and FC-ZFC curves of the two particles (few mg of samples) was measured at room temperature using a SQUID magnetometer (Quantum Design MPMS-XL). **Figure 1E** shows hysteresis loops of the samples in the field range of -500 to 500 Oe. Both samples have a small coercivity field (< 1 Oe, in the zoom-in profiles). Therefore, the particles exhibited superparamagnetic property at room temperature. At 500 Oe, the magnetization of MNPs and core/shell was 7.3 emu/g and 1.9 emu/g, respectively. This is because the silica shell has a small magnetization compared to the core alone, resulting in a lower mass susceptibility. The

susceptibilities ($\chi_r = \frac{M}{H}$) of core and core/shell particles were $0.183 \times 10^{-3} \text{ m}^3/\text{kg}$ and $0.048 \times 10^{-3} \text{ m}^3/\text{kg}$, respectively.

The ZFC and FC curves, shown in **Figure 1F**, were measured at temperatures from 5 to 300 K under a small applied magnetic field of 20 Oe. There are two different behaviors of magnetization in the ZFC-FC curves. Thermal hysteresis (memory effect) of the magnetization was observed only at the highest temperatures. This behavior is due to the phase transition between superparamagnetic and ferromagnetic character. The temperature of separation of the two phases is identified at the peak of the ZFC curve, known as blocking temperature (T_b), which was 213 K for core and 215 K for core/shell particles. The small difference of T_b between core and core/shells could be due to temperature errors of the measurement system or to a synergetic effect of the core/shell system.

The low T_b of the core/shell particles (-58 °C) meets very well the requirements of bio-applications at positive temperatures, i.e. much higher than T_b , by ensuring that the CS particles will be in a superparamagnetic state and will therefore not aggregate, while retaining magnetization.

3.2. Structure elucidation of silanized trans-resveratrol derivatives

The covalent bond process of the silane-derivative linker and *trans*-resveratrol molecules was inspected by observing the appearance of the C=O group at 1700 cm^{-1} and the disappearance of NCO group at 2270 cm^{-1} in the FT-IR transmittance spectra (**Figure 1** of supporting information). It is to be noted that, as compound **1** was always the dominant product even at the early stage of the reaction, we used an excess of *trans*-resveratrol compared to (triethoxysilyl)propyl isocyanate to obtain compound **3**. The structures of three main products (**Figure 2** of supporting information) were elucidated by NMR (Appendix 5 of

supporting information) and their molecular weight were determined by mass spectroscopy (Appendix 6 of supporting information).

In the $^1\text{H-NMR}$ spectra of **1**, all signals of three OH groups disappeared at 9-10 ppm. However, only one signal of the hydrogen atom of -OH group at 9.65 ppm was observed in the $^1\text{H-NMR}$ spectrum of **2**, and two -OH signal at 9.20 was observed in compound **3**. These data allow us to confirm that -OH functional positions of *trans*-resveratrol frameworks in **1**, **2**, and **3** were modified with three, two, and one substituted groups, respectively. Also, the signals of -NH group emerged at 7.7-7.8 ppm in the $^1\text{H-NMR}$ spectra, and signals of C=O bond at 154 ppm in the $^{13}\text{C-NMR}$ spectra are the evidence for the existence of the carbamate group of **1**, **2**, and **3**. The signals of linear hydrocarbons in the structure of 3-(triethoxysilyl)propyl isocyanate were found on the $^1\text{H-NMR}$ spectra at 1 to 4 ppm and $^{13}\text{C-NMR}$ spectra at 7 to 60 ppm with the proper ratio for 3, 2, and 1 substituted groups.

Precisely, the two-dimension NMR spectra of compounds **2** and **3** were tested to pinpoint the -OH conjugated position. The signal of -OH group appearing at 9.65 ppm on the proton spectrum of compound **3** proved that the two hydroxyl groups remained on the A ring of *trans*-resveratrol. Moreover, HMBC spectra showed the coupling of C-4' with H-3' and H-5' and the drop of the chemical shift of C-4' from 157.4 ppm to 151.1 ppm revealed the substitution of -OH at C-4' position of compound **3**. The structure of compound **2** was elucidated by the key couplings between protons and carbons on the HMBC spectrum: i) -OH (9.65 ppm) with C-4, and C-6 proved the presence free of hydroxyl group on the A ring; ii) H4 (6.41 ppm), H-2 and H-6 with C-3 and C-5 show that one hydroxyl group of A ring is substituted and makes the imbalance of A ring, therefore C-3 and C-5 have the different chemical shift, 154.3 ppm, and 158.2 ppm, respectively; iii) H-3' and H-5' with C-4' on the B ring prove the -OH at C-4' is modified with the chemical shift decrease of C-4' from 157.4 ppm in the *trans*-resveratrol structure to 150.7 ppm of compound **2**.

In conclusion, NMR characterization showed that compound (**1**) corresponds to 3',4,5'-tri((3-(triethoxysilyl)propyl)carbamate)-*trans*-stilbene, compound (**2**) is 5'-hydroxy-4-((3-(triethoxysilyl)propyl)carbamate)-3'-bis((3-(triethoxysilyl)propyl)carbamate)-*trans*-stilbene, and finally, compound (**3**) is 3',5'-dihydroxy-4-((3-(triethoxysilyl)propyl)carbamate)-*trans*-stilbene.

3.3. Functionalization of nanoparticles with silane-trans-resveratrol derivatives

To evaluate the success of *trans*-resveratrol grafting on nanoparticles, UV-Vis spectra were recorded (**Figure 2B**). Three distinct spectra with maximum wavelengths at 298 nm, 308 nm, and 302 nm were observed for **CS1**, **CS2**, and **CS3**, respectively, which corresponded to the absorbance band of *trans*-resveratrol (27, 28). More detailed analyses of UV-cross section extinction spectra are provided in **Figure 5** and will be discussed later.

In parallel, we compared the FTIR transmittance spectra of **CS1**, **CS2**, **CS3**, and the pristine **CS** in **Figure 2C**. In the four spectra, similar bands were observed at 900 - 1200 cm^{-1} and 1634 cm^{-1} , corresponding to the Si-C bond overlap with the Si-O band and the deformation of the vibration of adsorbed water molecules on the silica shell (29), respectively. Additional peaks at 1717 cm^{-1} (**CS1** and **CS2**) and 1709 cm^{-1} (**CS3**) corresponded to C=O bonds of in frameworks of **1**, **2**, **3**. These findings were consistent with a successful covalent coating of core/shell nanoparticles surfaces with *trans*-resveratrol. The slight differences between the wavenumber of the maximum absorption of the C=O band in the IR spectra **CS1**, **CS2**, and **CS3** and between the maximum wavelengths on the UV-Vis spectra could reflect conformation changes of silane-resveratrol derivatives when they were coated with a silica shell and/or the position of silane that was grafted.

3.4. Impact of pH of the aqueous TRIS buffer on nanoparticle aggregation

DLS measurements were carried out to examine the colloidal stability of nanoparticles within the 3.0 - 10.0 pH range generally used for in *vitro* protein interaction studies. The correlation coefficient increases with nanoparticle size or upon particle aggregation, and which is associated with a slower diffusion speed of particles. In **Figure 3**, the nearly single exponential decay of the autocorrelation function suggests a narrow distribution of **CS** sizes in the suspension. **Figure 3** evidenced that **CS**, **CS1**, **CS2** and **CS3** are monodisperse at pH 10.0. Resveratrol grafting onto **CS** has a negligible effect on the hydrodynamic radius (105, 120 and 100 nm for **CS1**, **CS2**, and **CS3**, respectively) at this alkaline pH value. At pH 10.0, nanoparticles dispersed in absolute ethanol had the same size distribution as in TRIS buffer, which evidenced their monodispersed colloidal behavior (see **Figure 3** of supporting information). Since **CS1** has 3 silane groups grafted on silica shell, **CS1** may potentially react with one or two neighboring nanoparticles during the functionalization step, resulting in nanoparticle covalent dimers and trimers (clusters) of around 200 nm or 300 nm diameter, respectively, whereas the non-reacting **CS1** remains as a single nanoparticle of 95-100 nm diameter. Similarly, **CS2** has 2 silane groups and may form covalent dimers. The DLS analysis of **CS1** and **CS2** suspended in alkaline TRIS buffer (pH 10.0) revealed that dimers and trimers may exist only in very negligible proportions. **CS1**, **CS2**, and **CS3** populations can thus be considered as a population of single nanoparticles after their functionalization.

From neutral to acidic conditions, the d_H distribution of **CS** shifted drastically and widened up to 800 nm, evidencing an aggregation process during acidification. The highest d_H value was reached for the most acidic condition. Indeed, the dispersed state vanished as soon as pH decreased below 7.0. This aggregation was fully reversible when alkalized with NaOH (data not shown). The three functionalization types resulted in three distinct aggregation behaviors. The mean d_H of aggregates depended on pH value, but differently, without conforming to one general pattern. An intermediate average diameter of aggregates was observed at pH 7.0 for **CS2** and **CS3**.

As shown in **Figure 4**, the mesoporous silica core/shell nanoparticles synthesized in this work exhibited a weak positive zeta-potential at pH 3.0, monotonously decreasing with increasing pH. In alkaline conditions, monodispersed **CS** exhibited a zeta-potential value of -27.7 ± 6.4 mV. Functionalization by resveratrol-silane derivatives significantly increased the negative value of the zeta-potential of **CS1**, **CS2**, and **CS3**. The most negative value was obtained for **CS3**, which contained the resveratrol-silane derivative with two free hydroxyls on one of its two phenolic groups and was also deprotonated at pH 10.0. In neutral and acidic conditions, the low zeta-potential values corresponded to those of nanoparticle aggregates of an average d_H up to 825 nm diameter.

Extinction cross-section spectra of **CS**, **CS1**, **CS2**, and **CS3** have been recorded both in clear bottom microplates using the Enspire plate reader in absorbance mode (**Figure 5**) and in quartz-cuvettes with a UV-1800 spectrophotometer (not shown), giving equivalent results. Extinction cross-section spectra of **CS** conformed to an exponential decrease of the wavelength for all the TRIS buffer pH values tested, fitting very well to the Rayleigh-Gans-Debye model (3.13) (30):

$$A_s(\lambda) = W \cdot \lambda^{-n} \quad (3.13)$$

Constants W and n were deduced from the linear fitting of the logarithm of extinction as a function of the logarithm of wavelength (Table S3.1 in the supporting information). Extinction cross-section intensity $A(\lambda)$ increased with pH value for a wavelength between 240 and 500 nm (**Figure 5**). Scattering fits were underestimated below 280 nm (**Figure 5**), with small negative values, showing that scattering and absorbance cross-section could not be accurately assessed in the [230-280 nm] wavelength domain with the Enspire reader plate. We also noticed that compared to **CS**, silane-resveratrol grafted nanoparticles displayed an additional absorbance maximum centered at 315-320 nm. The absorbance value increased with pH, which is also the case of free *trans*-resveratrol between pH 5.0 and 10.0 (31). The absorbance maximum was different for the three grafted types due to the different substitution and grafting.

4. Discussion

Mesoporous silica exhibits four types of silanol groups, which can be separately studied by both NMR (32, 33) and vibrational infrared spectroscopy (34). They exhibit contrasted acidity and chemical reactivity (35-37). Single silanol groups, designated as isolated silanols (Q^3), with three covalent Si-O links with the bulk silica, are located at a far distance from neighboring H-donors or H-acceptors, which prevents hydrogen bonding. Q^3 are the most acidic silanols (pK_a around 4.8) and therefore become the first deprotonated sites at pH 5.0. They are followed by hydrogen-bonded vicinal (Q^1) and geminal (Q^2) silanols, which have an intermediary acidity ($8.5 < pK_a < 9.3$) and are progressively deprotonated between pH 7.0 and pH 10.0. Finally, inner silanols (Q^4) are the least acidic ones ($pK_a > 11.0$). They thus remained always protonated in the pH range of our experiments (3.0 and 10.0) (37).

Consequently, as observed on **Figure 4** describing the pH-dependence of the zeta-potential, the surface charge density of **CS** remained very reduced at pH 3.0 and therefore the electrical double layer repulsion of counter-ions had a very weak strength. Then, attractive forces between nanoparticles such as van der Waals dispersion forces became sufficient for spontaneous nanoparticle aggregation (38). Depending on the three functionalization types studied, phenolic groups of two neighboring nanoparticles could also be submitted to additional interaction forces, in particular π - π stacking forces. They may explain differences in aggregation processes (reaction-limited and diffusion-limited cluster aggregation) and in morphology (compactness, shape, gyration radius), resulting in contrasted d_H distributions between **CS1**, **CS2**, and **CS3**. In the case of **CS3**, the presence of the resorcinol group at their surface may also create a specific affinity site for the silica surface of the neighboring nanoparticles (39). Indeed, catechol, a position isomer of resorcinol, is adsorbed more easily than water onto silica surface due to the specificities of its hydrogen bonding (40).

The distribution of the more acidic silanol groups on the mesoporous silica surface may be possibly heterogeneous, at the origin of the puzzle of more negative areas and more positive areas as pH increased. Electrostatic forces increased with the deprotonation of the surface silanols and may participate in repulsive forces between nanoparticles. Finally, when the majority of Q² and Q³ silanols became deprotonated, the surface charge density became high and the long-range electrostatic repulsion of counterions became strong enough to stabilize the water suspensions in a monodispersed state, even at high ionic strength. This pH-dependent charge density of **CS** was observed in the case of many metal oxides: α -quartz and α -cristobalite (41), α -alumina (42), smectite (43), illite (44), magnetite Fe₂O₃ (45), maghemite Fe₂O₃ (46), titanium oxide (TiO₂) (45), zinc oxide (ZnO) (45).

Interestingly, the zeta-potential of coated nanoparticles became more negative than the **CS** net charge with the increase of the pH value. The surface charge of metal oxides originates from four major mechanisms (45): (1) the isomorphous substitution of structural Si⁴⁺ by cations of lower valence (Al³⁺, Fe³⁺, Zn³⁺ ...) creates structural charges which are pH-independent; (2) under-coordinated Si⁴⁺ of silica layer edges hydrate into silanols in an attempt to complete their coordination sphere. Usually, siloxanes of surface layers are potentially partially oxidized in silanol when they experienced a rich O₂ medium. Protonations/deprotonations of interfacial silanols generate charges depending on the aqueous pH buffer; (3) some charges also originate from additional lattice imperfections and impurities; (4) finally, interfacial complexation of protons or other ions also occurs within the inner-sphere or the outer-sphere complexes.

In a future work, using small amounts of nanoparticles, vibrational infrared spectroscopy could be used to assess silanol proportions. Indeed, changes in their proportion should induced changes in absorption bands at 3747 cm⁻¹ (isolated silanol), at 3660 and 3620 cm⁻¹ (vicinal silanol), at 3740 cm⁻¹ (germinal silanol), and at 1110, 1050, 1085 cm⁻¹ (siloxane) (47). Using many nanoparticles, solid-state NMR of ²⁹Si could reveal if the number of silanols and their Q²-Q³-Q⁴ proportions are modified after the three functionalizations (**CS1**, **CS2**, **CS3**), resulting in an average pK_a shift. Finally, potentiometric acidity titration may also highlight surface charge density of functionalized nanoparticles.

5. Conclusion

This work reports the preparation of novel magnetic nanoparticles grafted with *trans*-resveratrol derivatives and their aggregation behavior in an aqueous environment. Thanks to their superparamagnetic property, MNPs coupled with *trans*-resveratrol could be a potential candidate for ligand fishing and screening of proteins. Three *trans*-resveratrol derivatives were synthesized, purified and their structures were identified before their grafting on the surface of MNPs. This was an essential step for further understanding the interactions of these MNPs with protein. UV-Vis spectra indicated that *trans*-resveratrol was not isomerized into *cis*-resveratrol during the preparation process. The colloidal behavior/aggregation of these nanoparticles in aqueous solution is mainly governed by pH. They are monodispersed at pH 10.0 and tend to aggregate at neutral and acidic pH, due to the decrease of the surface charge density (assessed by zeta potential measurement), resulting in lower electrostatic repulsion forces. The aggregation process results in the decrease of the extinction cross-section, mainly due to the decrease of the light scattering cross-section. A negligible difference in aggregation behavior was observed between uncoated and coated nanoparticles. The understanding of the aggregation behavior of nanoparticles in aqueous solution at different pH is important for their uses in quantitative applications.

Declarations

Availability of data and materials

Figure data are available on request

Competing interests

The authors declare that they have no competing interests

Authors' contributions

Thi-Nga Nguyen synthesized nanoparticles grafted with *trans*-resveratrol derivatives, carried out the aggregation study, and wrote the original draft. Quang-Hung Tran and Ferial Terki investigated the magnetic property, edited the manuscript, and supervised this work. Clarence Charnay and Xavier Dumail trained and supported for nanoparticle synthesis. Corinne Reibel carried out the SQUID measurements. Guillaume Cazals and Gilles Valette carried out and interpreted data of mass spectroscopy. Christian Jay-Allemand and Luc P. R. Bidet conceived, supervised this study, and revised the manuscript.

Acknowledgements

We are grateful to Prof. Eric Dubreucq (Institut Agro, Montpellier) for his critical reading and correction of this manuscript. Thi-Nga Nguyen would like to acknowledge the Medicinal Chemistry Project of Vietnam ((No. 4772/QĐ/BGDĐT) and Campus France (No. 883333H) for the funding of her Ph.D. in France.

References

1. Lacroix S, Klicic Badoux J, Scott-Boyer MP, Parolo S, Matone A, Priami C, et al. A computationally driven analysis of the polyphenol-protein interactome. *Sci Rep-Uk*. 2018;8(1):2232.
2. Costa G, Francisco V, C. LM, Cruz MT, Batista MT. Intracellular signaling pathways modulated by phenolic compounds: Application for new anti-inflammatory drugs discovery. *Current Medicinal Chemistry*. 2012;19:2876-900.
3. Shukor AN, Raes K, Van Camp J, Smagghe G. Analysis of interaction of phenolic compounds with the cholecystokinin signaling pathway to explain effects on reducing food intake. *Peptides*. 2014;53:225-31.
4. Lattanzio V, Lattanzio VMT, Cardinali A. Role of polyphenols in the resistance mechanisms of plants against fungal pathogens and insects. In: Imperato F, editor. *Phytochemistry: Advances in Research: Research Signpost*; 2006. p. 23-67.
5. Baur JA, Sinclair DA. Therapeutic potential of resveratrol: The *in vivo* evidence. *Nature Reviews Drug Discovery*. 2006;5(6):493-506.
6. Woodby B, Penta K, Pecorelli A, Lila MA, Valacchi G. Skin health from the inside out. *Annual Review of Food Science and Technology*. 2020;11:235-54.
7. Quideau S, Deffieux D, Pouysegu L. Resveratrol still has something to say about aging! *Angew Chem Int Ed Engl*. 2012;51(28):6824-6.
8. Frankel EN, Waterhouse AL, Kinsella JE. Inhibition of human LDL oxidation by resveratrol. *The Lancet*. 1993;341:1103-4.
9. Soleas GJ, Diamandis EP, Goldberg DM. The world of resveratrol. In: research Aifc, editor. *Nutrition and cancer prevention Advances in experimental medicine and biology*. 492: Springer, Boston, MA; 2001. p. 159-82.
10. Koushki M, Amiri-Dashatan N, Ahmadi N, Abbaszadeh HA, Rezaei-Tavirani M. Resveratrol: A miraculous natural compound for diseases treatment. *Food Science and Nutrition*. 2018;6(8):2473-90.
11. Jung HJ, Hwang IA, Sung WS, Kang HJ, Kang BS, Seu YB, et al. Fungicidal effect of resveratrol on human infectious fungi. *Archives of Pharmal Research*. 2005;28(5):557-60.
12. Schouten A, Wagemakers L, Stefanato FL, Kaaij RM, Kan JAL. Resveratrol acts as a natural profungicide and induces self-intoxication by a specific laccase. *Molecular Mircobiology*. 2002;43(4).
13. Vestergaard M, Ingmer H. Antibacterial and antifungal properties of resveratrol. *International Journal of Antimicrobial Agents*. 2019;53(6):716-23.
14. Pharm RPB, Sahni JK, Ali J, Sharma S, Baboota S. Resveratrol: Review on therapeutic potential and recent advances in drug delivery. *Expert Opinion on Drug Delivery*. 2014;11(8):1285-98.
15. Carmen L-An, Isabel F, Jose ML-N, Estrella N-D. Cyclodextrins as resveratrol carrier system. *Food Chemistry*. 2007;104:39-44.

16. Prakash J, Bothiraja C, Atmaram P. Resveratrol-piperine loaded mixed micelles: formulation, characterization, bioavailability, safety and in vitro anticancer activity. RSC Advances. 2016;6:112795.
17. Sabna K, Hibah M, Shaimaa MB-E, Nabil AA, Shabad M. Coconut oil-based resveratrol nanoemulsion: Optimization using response surface methodology, stability assessment and pharmacokinetic evaluation. Food Chemistry. 2021;357:129721.
18. Santos AC, Pereira I, Pereira-Silva M, Ferreira L, Caldas M, Magalhães M, et al. Nanocarriers for resveratrol delivery: Impact on stability and solubility concerns. Trends in Food Science & Technology. 2019;91:483-97.
19. Juere E, Florek J, Bouchoucha M, Jambhrunkar S, Wong KY, Popat A, et al. *In vitro* dissolution, cellular membrane permeability, and anti-inflammatory response of resveratrol-encapsulated mesoporous silica nanoparticles. Molecular Pharmaceutics. 2017;14(12):4431-41.
20. Popova M, Szegedi A, Mavrodinova V, Tušar NN, Mihály J, Klébert S, et al. Preparation of resveratrol-loaded nanoporous silica materials with different structures. Journal of Solid State Chemistry. 2014;219:37-42.
21. Summerlin N, Qu Z, Pujara N, Sheng Y, Jambhrunkar S, McGuckin M, et al. Colloidal mesoporous silica nanoparticles enhance the biological activity of resveratrol. Colloids and Surfaces B: Biointerfaces. 2016;144:1-7.
22. Sallem F, Haji R, Vervandier-Fasseur D, Nury T, Maurizi L, Boudon J, et al. Elaboration of *trans*-resveratrol derivative-loaded superparamagnetic iron oxide nanoparticles for glioma treatment. Nanomaterials (Basel). 2019;9(2):287.
23. Zhuo R, Liu H, Liu N, Wang Y. Ligand fishing: A remarkable strategy for discovering bioactive compounds from complex mixture of natural products. Molecules. 2016;21(11):1516.
24. Nyalosaso JL, Rascol E, Pisani C, Dorandeu C, Dumail X, Maynadier M, et al. Synthesis, decoration, and cellular effects of magnetic mesoporous silica nanoparticles. RSC Advances. 2016;6(62):57275-83.
25. Elle RE, Rahmani S, Lauret C, Morena M, Bidel LP, Boulahtouf A, et al. Functionalized mesoporous silica nanoparticle with antioxidants as a new carrier that generates lower oxidative stress impact on cells. Molecular Pharmaceutics. 2016;13(8):2647-60.
26. Stetefeld J, McKenna SA, Patel TR. Dynamic light scattering: A practical guide and applications in biomedical sciences. Biophysical Reviews. 2016;8(4):409-27.
27. Camont L, Cottart CH, Rhayem Y, Nivet-Antoine V, Djelidi R, Collin F, et al. Simple spectrophotometric assessment of the *trans*-/*cis*-resveratrol ratio in aqueous solutions. Analytica Chimica Acta. 2009;634(1):121-8.
28. Trela BC, Waterhouse AL. Resveratrol: Isomeric molar absorptivities and stability. Journal of Agricultural and Food Chemistry. 1996;44:1253-7.
29. Chukin GD, Malevich VI. Infrared spectra of silica. Journal of Applied Spectroscopy. 1977;26:223-9.

30. Heirwegh KPM, Meuwissen JATP, Lontie R. Selective absorption and scattering of light by solutions of macromolecules and by particulate suspensions. *Journal of Biochemical and Biophysical Methods*. 1987;14:303-22.
31. Nicolas JML, Carmona FG. Aggregation state and pK_a values of (*E*)-resveratrol as determined by fluorescence spectroscopy and UV-visible absorption. *Journal of Agricultural and Food Chemistry*. 2008;56:7600-5.
32. Ide M, El-Roz M, De Canck E, Vicente A, Planckaert T, Bogaerts T, et al. Quantification of silanol sites for the most common mesoporous ordered silicas and organosilicas: Total versus accessible silanols. *Physical Chemistry Chemical Physics*. 2013;15(2):642-50.
33. Zhao H, Chen Q, Zhang S. A novel scheme for quantitative characterization of the structures of mesoporous silica by solid-state ^{29}Si NMR. *Microporous and Mesoporous Materials*. 2012;155:240-4.
34. Paukshtis EA, Yaranova MA, Batueva IS, Bal'zhinimaev BS. A FTIR study of silanol nests over mesoporous silicate materials. *Microporous and Mesoporous Materials*. 2019;288:109582.
35. Liu X, Cheng J, Lu X, Wang R. Surface acidity of quartz: Understanding the crystallographic control. *Physical Chemistry Chemical Physics*. 2014;16(48):26909-16.
36. Rimola A, Costa D, Sodupe M, Lambert JF, Ugliengo P. Silica surface features and their role in the adsorption of biomolecules: Computational modeling and experiments. *Chemical Reviews*. 2013;113(6):4216-313.
37. Sulpizi M, Gaigeot MP, Sprik M. The silica-water interface: How the silanols determine the surface acidity and modulate the water properties. *Journal of Chemical Theory Computation*. 2012;8(3):1037-47.
38. Hotze EM, Phenrat T, Lowry GV. Nanoparticle aggregation: Challenges to understanding transport and reactivity in the environment. *Journal of Environmental Quality*. 2010;39(6):1909-24.
39. Gunko VM, Silchenko SS, Bogomaz VI. Interaction of dihydrobenzenes with pyrogenic silica. *Theoretical and Experimental Chemistry*. 1991;27:619-25.
40. Mian SA, Yang LM, Saha LC, Ahmed E, Ajmal M, Ganz E. A fundamental understanding of catechol and water adsorption on a hydrophilic silica surface: Exploring the underwater adhesion mechanism of mussels on an atomic scale. *Langmuir*. 2014;30(23):6906-14.
41. Tang C, Zhu J, Li Z, Zhu R, Zhou Q, Wei J, et al. Surface chemistry and reactivity of SiO_2 polymorphs: A comparative study on α -quartz and α -cristobalite. *Applied Surface Science*. 2015;355:1161-7.
42. Ntalikwa JW. Determination of surface charge density of α -alumina by acid-base titration. *Bulletin of the Chemical Society of Ethiopia*. 2007;21(1):117-28.
43. Lützenkirchen J, Preočanin T, Bauer A, Metz V, Sjöberg S. Net surface proton excess of smectites obtained from a combination of potentiometric acid–base, mass and electrolyte titrations. *Colloids and Surfaces A: Physicochemical and Engineering Aspects*. 2012;412:11-9.
44. Du Q, Sun Z, Forsling W, Tang H. Acid–base properties of aqueous illite surfaces. *Journal of Colloid and Interface Science*. 1997;187:221-31.

45. Tombácz E. pH-dependent surface charging of metal oxides. *Periodica Polytechnica Chemical Engineering*. 2009;53(2):77-86.
46. Lucas IT, Vidal SD, Dubois E, Chevalet J, Turq P. Surface charge density of maghemite nanoparticles: Role of electrostatics in the proton exchange. *The Journal of Physical Chemistry C*. 2007;111:18568-76.
47. Carteret C. Etude, par spectroscopie dans le proche infrarouge, et modélisation des structures de surface et de l'hydratation de silices amorphes. France: Université Henri Poincaré Nancy 1; 1999.

Scheme

Scheme 1 is available in Supplemental Files section.

Figures

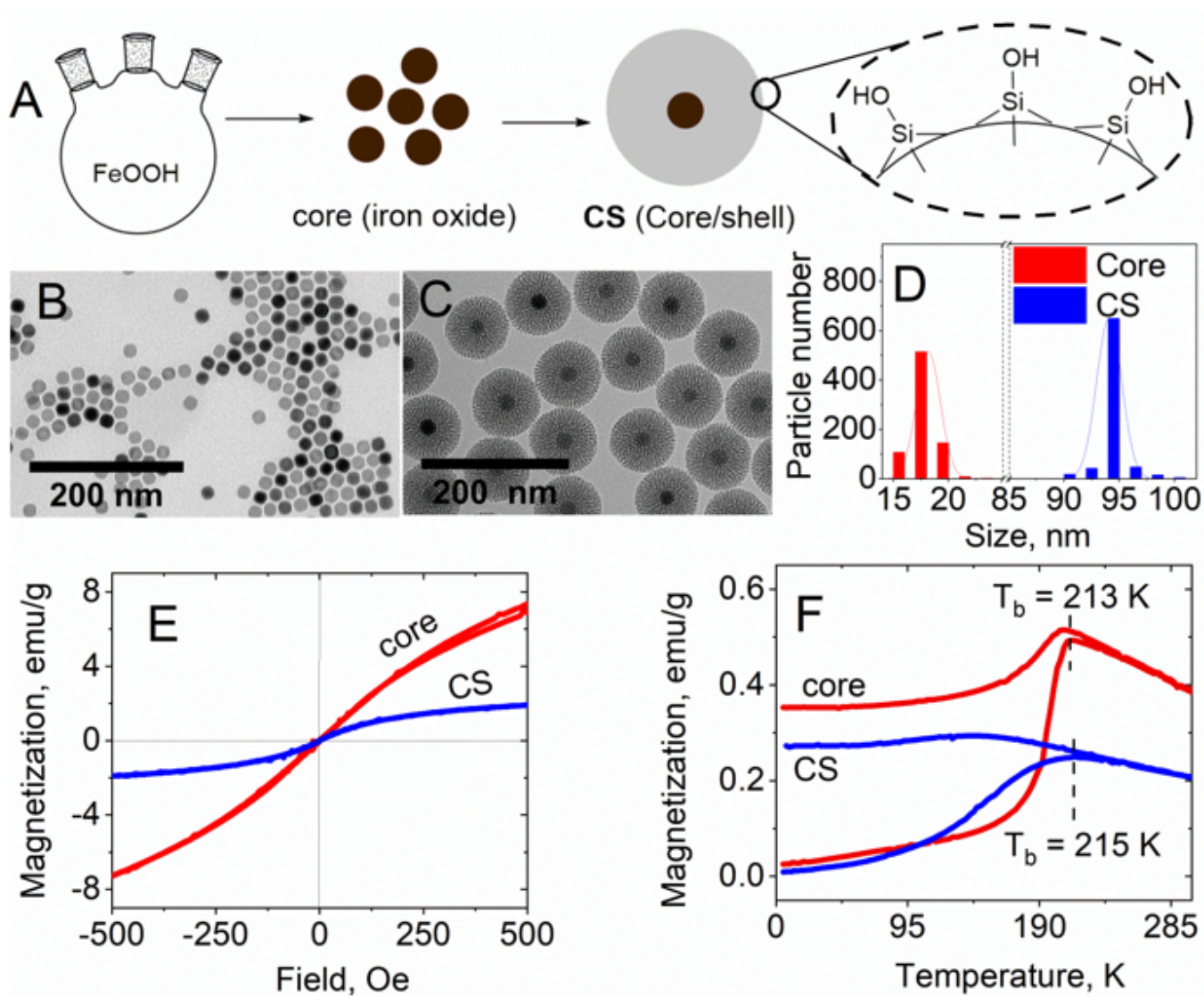


Figure 1

A: scheme of synthesis of particles with iron oxide core and mesoporous silica shell. The inset of the core/shell surface is shown on the right. B & C: TEM images of iron oxide (core) and core with silica shell (core/shell) nanoparticles. D: size distribution of the core and core/shell nanoparticles analyzed from TEM. E: magnetization curves of core and core/shell nanoparticles recorded at room temperature versus the applied field. F: magnetization measurements of core and core/shell particles as a function of temperature with an applied field of 20 Oe.

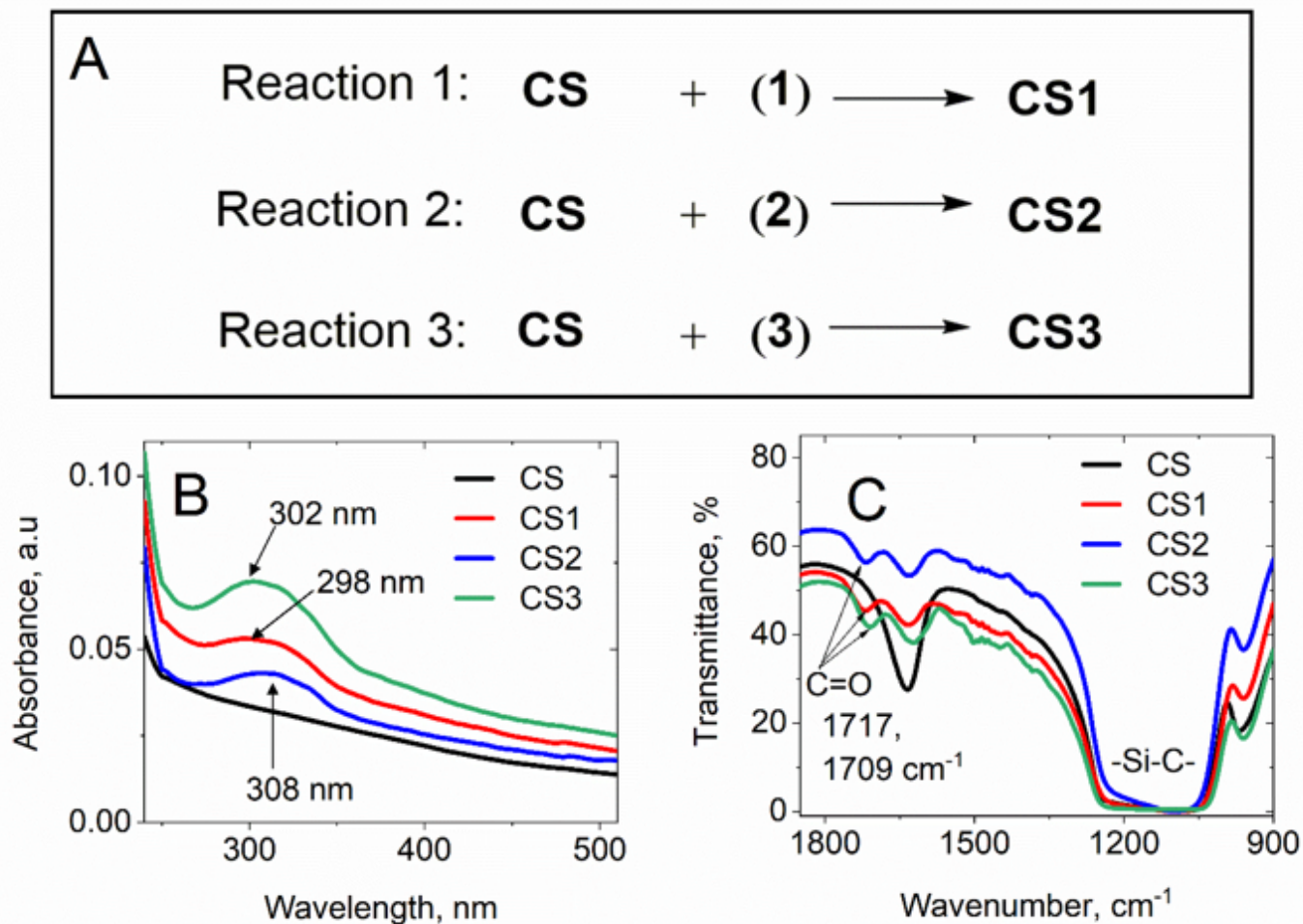


Figure 2

A: Scheme of synthesis of CS nanoparticles grafted with *trans*-resveratrol. B: UV-Vis spectra of the 3 types of grafted nanoparticles from 250 nm to 650 nm. C: The infrared spectra of core/shell grafted with 1, 2, 3 molecules corresponding to CS1, CS2, and CS3, respectively. Both UV-Vis and IR spectra of native CS (black curves) were plotted to observe the changes in absorbance and transmittance properties of the nanoparticles.

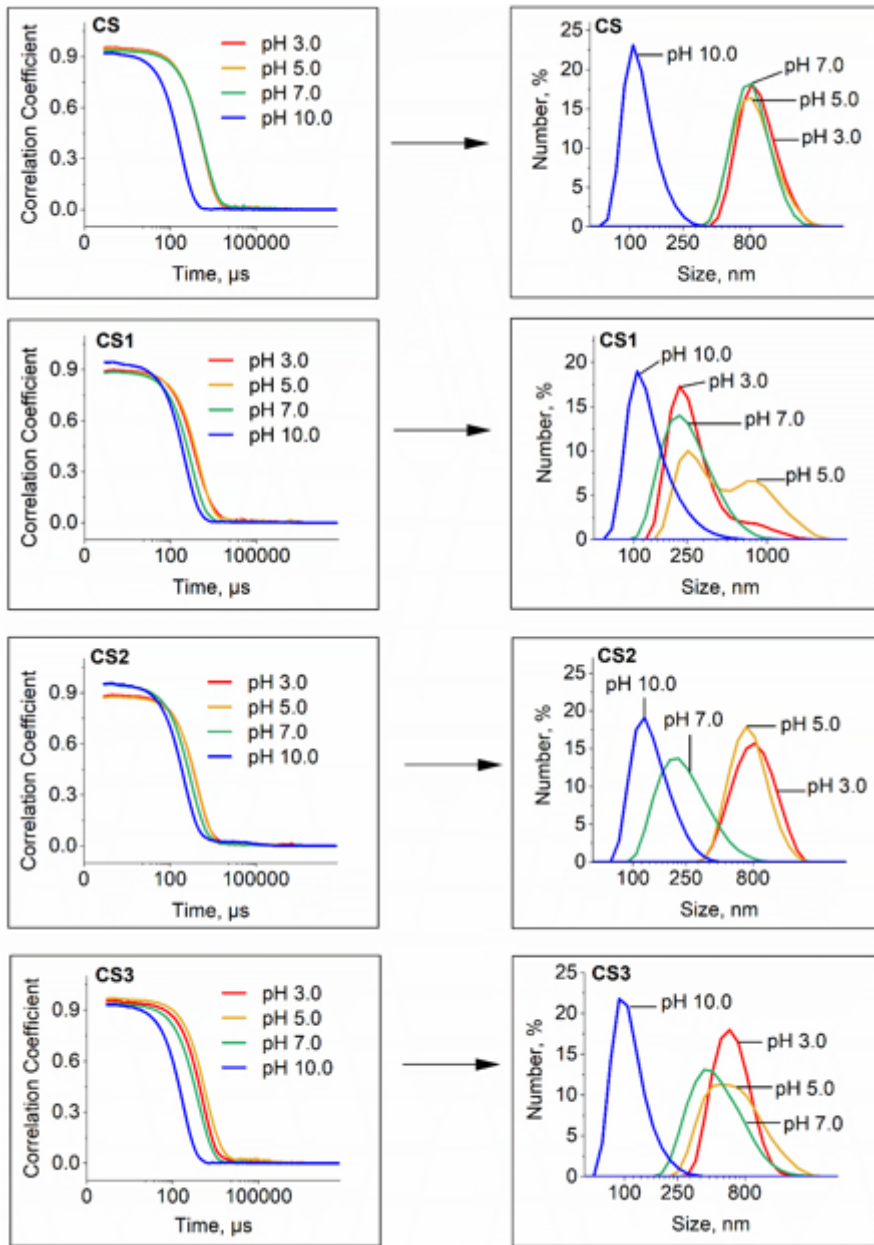


Figure 3

Correlation coefficient as a function of lag time (on the left) and size distribution (on the right) of uncoated and coated nanoparticles in TRIS buffer (50 mM) at different pH values, obtained by Dynamic Light Scattering.

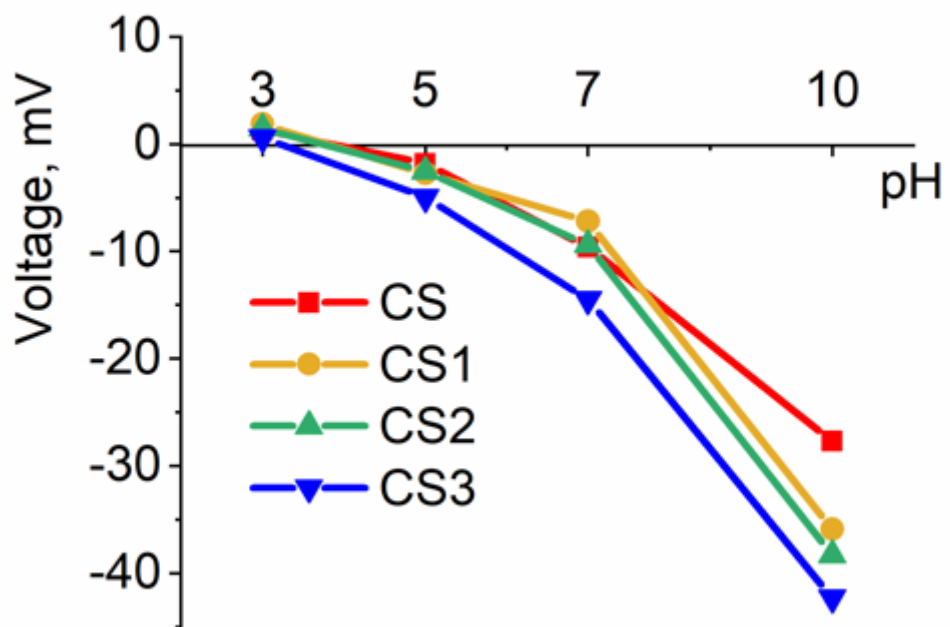


Figure 4

pH-dependence of zeta-potential at 25°C of CS, CS1, CS2 and CS3 suspended in TRIS buffer (50 mM) at concentration of 50 ppm (~ 50 μ g/mL). Each point was the mean of 5 replicates.

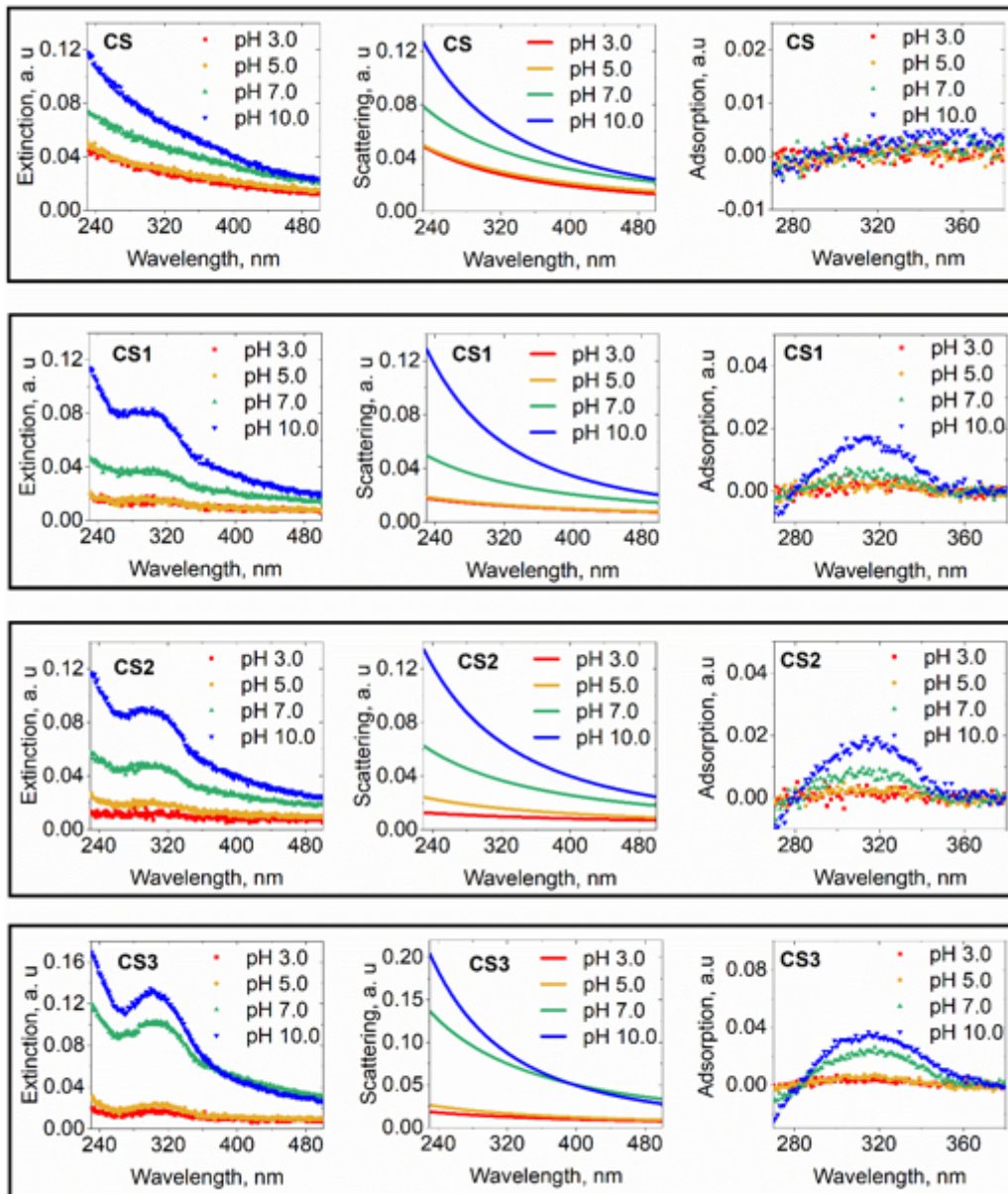


Figure 5

pH-dependence of extinction cross-section spectra of CS, CS1, CS2, and CS3 recorded using an EnSpire microplate reader (left column), with the subtraction of TRIS buffer extinction cross-section spectrum. In the central column, scattering cross-section spectra were fitted to . In the right column, adsorption cross-section spectra were deduced by subtraction . Scattering fits were overestimated below 280 nm, so that negative values of small intensities occurred, showing that scattering and absorbance cross-section could not be accurately assessed in the [230-280 nm] wavelength domain.

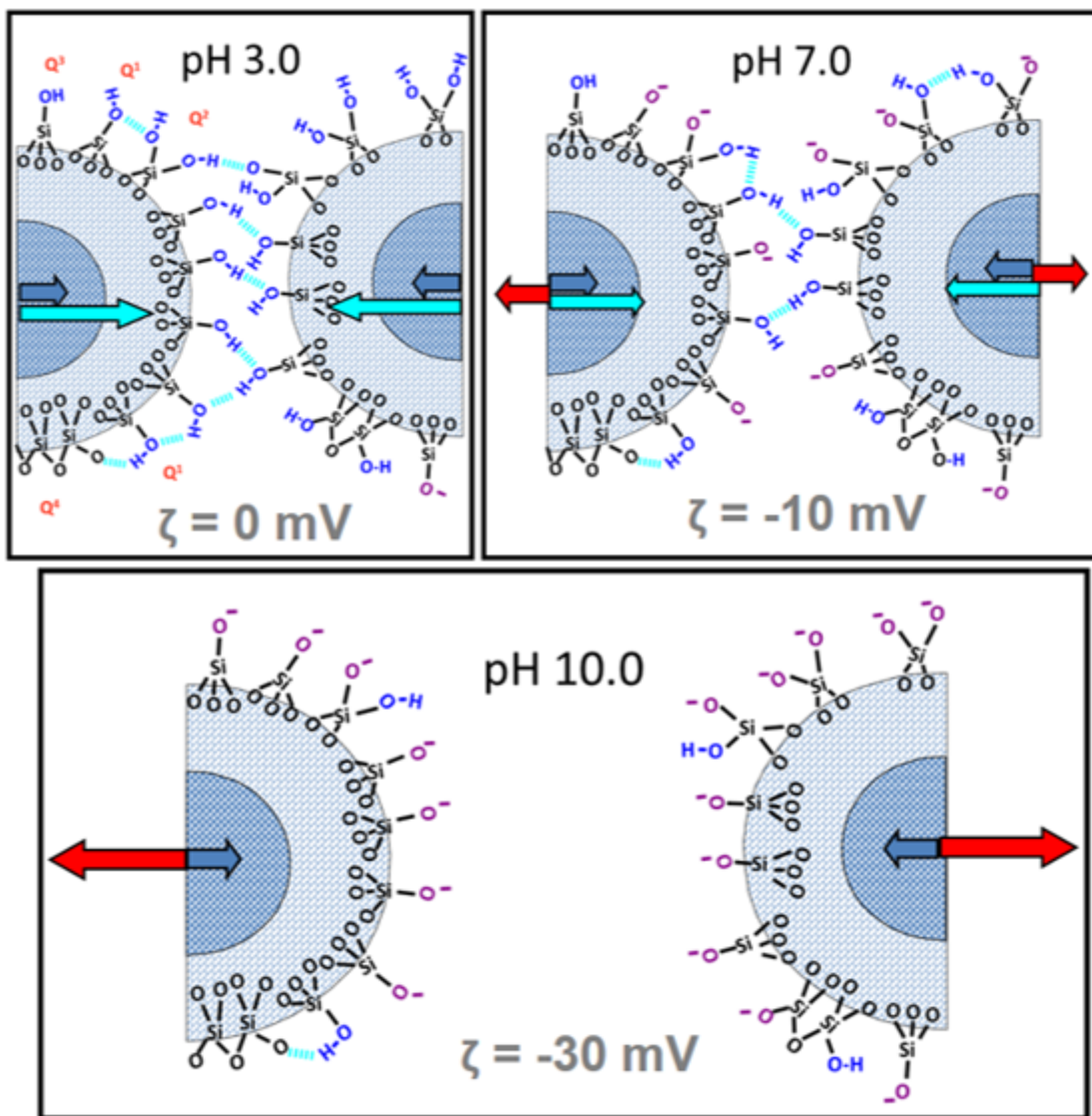


Figure 6

pH dependence of the aggregation behavior of nanoparticles in TRIS 50 mM buffer (pK_a 8.3). At pH 3.0 (zeta potential $\zeta \sim 0$), all silanols are protonated and van der Waals attractive forces between nanoparticles (blue arrow) are reinforced by interparticle hydrogen bonds (green arrow) formed between silanols. Solely a few isolated silanols (Q^3), which have the lowest pK_a , are deprotonated. At pH 7.0 ($\zeta = -10$ mV), isolated (Q^3), vicinal (Q^1) and germinal (Q^2) silanols tend to be deprotonated so that a well-formed counter-ion layer exerts a repulsive force (red arrow) on nanoparticles. Interparticle hydrogen bonds also decrease at pH 7.0. At pH 10.0 ($\zeta = -30$ mV), all silanols are deprotonated and the counter-ion layer is fully developed, exerting higher repulsive forces, and preventing aggregation. The magnetic attraction force is negligible due to super-paramagnetism property at room temperature.

Supplementary Files

This is a list of supplementary files associated with this preprint. Click to download.

- [SupportingInformation26012022.docx](#)
- [Scheme1.png](#)